Controllable adhesion using field-activated fluids

Randy H. Ewoldt*
Institute for Mathematics and its Applications
& The Department of Chemical Engineering and Materials Science,
University of Minnesota, 207 Church Street S.E.,
Minneapolis, Minnesota 55455, USA

Piotr Tourkine, Gareth H. McKinley, and A. E. Hosoi†
Hatsopoulos Microfluids Laboratory, Department of Mechanical Engineering,
Massachusetts Institute of Technology, 77 Massachusetts Avenue, Cambridge, Massachusetts 02139, USA
(Dated: Initially Submitted 20 August 2010)

We demonstrate that field-responsive magnetorheological (MR) fluids can be used for variable-strength controllable adhesion. The adhesive performance is measured experimentally in tensile tests (a.k.a. probe-tack experiments) in which the magnetic field is provided by a cylindrical permanent magnet. Increasing the magnetic field strength induces higher peak adhesive forces. We hypothesize that the adhesion mechanism arises from the shear resistance of a yield stress fluid in a thin gap. This hypothesis is supported by comparing the experimentally measured adhesive performance to the response predicted by a lubrication model for a non-Newtonian fluid with a field-dependent yield stress. The model predictions are in agreement with experimental data up to moderate field strengths. Above a critical magnetic field strength the model over-predicts the experimentally measured values indicating non-ideal conditions such as local fluid dewetting from the surface.

I. INTRODUCTION

Viscous Newtonian fluids confined in sufficiently small gaps can provide strong resistance to the separation of two parallel rigid surfaces, a phenomenon known as Stefan adhesion [1]. This type of Newtonian fluid adhesion is important in understanding "tackiness" [2, 3], but is limited in application because a finite separation velocity is required to induce adhesive Newtonian stresses.

In contrast, a suitably non-Newtonian fluid – e.g. a yield stress fluid [4, 5] – can provide adhesive force even under static conditions. Yield stress fluids are materials which approximately behave as a solid below a critical stress condition, flow as a liquid for larger stresses, and can repeatedly and reversibly transition between these solid-like and liquid-like states. A yield stress fluid can therefore be interpreted as an extreme case of non-Newtonian shear-thinning viscosity. The adhesive quality of yield stress fluids can be readily observed in peanut butter, whipped cream, or toothpaste. In biology, yield stress fluid adhesion is thought to be the attachment mechanism of wall-climbing snails and slugs [6], and engineered devices have recently been inspired to exploit yield stress fluid adhesion as a locomotion strategy to climb walls [7, 8]. Confined yield stress fluids have been studied under tensile loading [9, 10] and compressive squeeze flow, e.g. [11–14]. The tensile adhesive performance is directly related to the yield stress of the fluid, which typically exhibits isotropic properties [15].

Field-responsive or so-called "smart" yield stress fluids are also available, which exhibit a variable microstructure (and yield stress) as a function of the applied external field, e.g. magnetic or electric. Many field-responsive materials and structures exist [16], but here we focus on magnetorheological (MR) fluids. MR fluids typically consist of a suspension of non-colloidal ferromagnetic particles. An external magnetic field induces magnetic dipoles in the particles, causing them to form chains along field lines. This field-aligned anisotropic configuration strongly resists shear deformation with displacements perpendicular to the field lines, and most studies and applications subject MR fluids to shear loading. Only a few results have been published on tensile loading of MR fluids, such as experimental studies of oscillatory squeeze flow [17] and theoretical modeling of tensile adhesion [18], but the true efficacy of tensile adhesive loading for a field-responsive yield stress fluid is an open question which we address in this work.

The prospect of utilizing MR fluids for tensile adhesion is compelling, since this would allow for controllable, tunable, and reversible attachment. As an additional practicality, adhesion to arbitrary surfaces (such as walls or windows) requires that the field source be located on only one side of the fluid, thus inhibiting the option of creating a homogeneous magnetic field condition. As a consequence, functional MR fluid adhesion must tolerate a nonhomogeneous magnetic field.

Here we demonstrate experimentally that MR fluids can be used with nonhomogeneous fields (e.g. created by a permanent magnet that is placed near a drop of the MR fluid) to attach to non-ferromagnetic substrates including plastic, aluminum, ceramic tile, and wood. Fig. 1 demonstrates the feasibility of using magnetic fields for switchable adhesion to various nonmagnetic substrates.

Adhesive performance will depend on the method of

*Electronic address: ewoldt@ima.umn.edu
†Electronic address: peko@mit.edu

FIG. 1: Demonstration of reversible adhesion to nonmagnetic substrates using field-activated magnetorheological (MR) fluid. Surfaces shown are wood, aluminum, and ceramic tile, demonstrating adhesion across a range of substrate surface roughness. The suspended mass, $m = 112$ g, is a switchable permanent magnet configuration which creates a magnetic field strength on the order of $B = 0.16$ T over an area of approximately $A \approx 230$ mm^2. The holding stress is therefore at least $mg/A \approx 4.8$ kPa.

separation of the two surfaces, such as normal pull-off, shearing, or peeling [19]. Here experimental results are reported for both normal and shear loading of a field-responsive yield stress fluid confined between rigid surfaces, as the external magnetic field and the geometry of the adhesive contact are varied. The peak adhesive force and the mode of failure are all controlled by the field-responsive nature of the magnetorheological fluid comprising the adhesive layer. Using a combination of experimental measurements and non-Newtonian lubrication flow modeling, we argue that the mechanism of this tensile adhesion is due to the field-responsive shear yield stress of the magnetorheological fluid.

II. BACKGROUND: FLUID ADHESION

Consider a fluid confined in a small gap ($h/R \ll 1$) between rigid parallel surfaces, as shown in Fig. 2. Both capillary forces and bulk viscous stresses resist separation of the plates. The capillary force on a bounding surface, assuming an axially and vertically symmetric meniscus, is given by [20]

$$F_{\text{Capillary}} = \frac{\gamma}{h/2}\cos\theta_E(\pi R^2) + \gamma \sin\theta_E(2\pi R) \qquad (1)$$

where γ is the surface tension and θ_E is the contact angle. Eq. 1 is the superposition of a capillary pressure difference within the fluid and the line traction at $r = R$. For a wetting fluid $\theta_E < 90°$ and the fluid acts to pull the plates together. Under static conditions the pressure profile in the fluid is constant as a function of the radius, $p(r) \sim r^0$, since no other forces exist in the radial direction. The pressure differential across the curved interface will dominate when $R/(h\tan\theta_E) > 1$, which is generally the case of a single wetting droplet confined in a small gap, but for an array of discrete droplets the line traction will be multiplied by the number of droplets and can become dominant [21].

Bulk material stresses will also resist separation of the plates. For a viscous fluid, material stresses will result

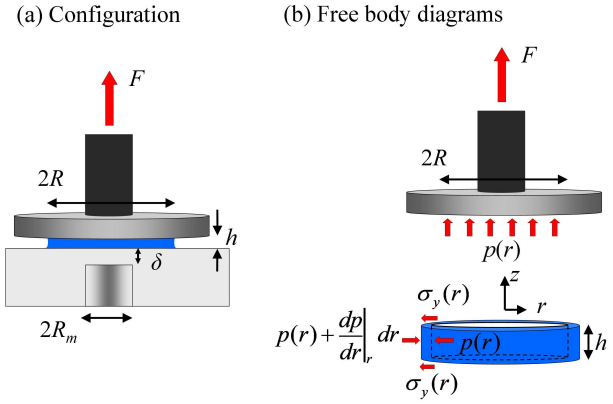

FIG. 2: (a) Sketch of the experimental setup for adhesive pull-off tests of a field-responsive magnetorheological fluid. Instrument materials are non-magnetic. The adhesive fluid layer (radius R, gap height h) resides between rigid surfaces. The lower plate has a cavity to allow a permanent magnet (radius R_m) to be introduced to "activate" the adhesive with a nonhomogeneous field. The top of the magnet is separated from the bottom of the fluid by a distance δ. (b) Free body diagrams for yield stress fluid adhesion. For the top plate only forces in the z-direction are shown. For the fluid, the shape of the control volume is a ring. The fluid is modeled locally as a perfect plastic with a radially dependent yield stress. Small gaps are assumed ($h/R \ll 1$), so that material deformation consists primarily of shear.

when the plates are separated at finite velocity. As the (thin) gap increases, conservation of volume requires the fluid to flow radially inward, and the no-slip condition at the surfaces creates a shear gradient in the z-direction. This inward shear flow requires a radial pressure gradient, such that the pressure in the fluid is below ambient. This resulting negative gauge pressure tends to pull the plates together, resisting separation and acting adhesively. The classic problem of "Stefan adhesion" [1, 22] considers the case of an incompressible Newtonian fluid in the limit of small gaps ($h/R \ll 1$). For quasi-static loading conditions we neglect the inertia of the solid components. This assumption should be checked [23, 24]; for our experiments, $\dot{h} = 10\mu m/s$, $\ddot{h} \sim 10\mu m/s^2$ from analysis of typical data (where the dot indicates a time derivative), and a system mass M of a few hundred grams gives $M\ddot{h} \sim 3\cdot 10^{-6}$ N. This is much less than any experimentally measured force, therefore the measured load F is balanced only by the material stress. Neglecting system inertia, the momentum balance in the z-direction is determined by the free body diagram shown in Fig. 2b, resulting in

$$F = -2\pi \int_0^R p(r) r dr \qquad (2)$$

where $p(r)$ is the gauge pressure relative to atmospheric conditions outside of the fluid. Positive adhesive forces, $F > 0$, correspond to negative pressures in the fluid, and

negative pressure (positive radial pressure gradient) must exist to drive fluid flow inward. For a Newtonian fluid at low Reynolds number with $h/R \ll 1$, the quasi-steady lubrication approximation is valid, and the momentum balance in the r-direction simplifies to

$$\frac{\partial p}{\partial r} = \mu \frac{\partial^2 v_r}{\partial z^2} \tag{3}$$

where μ is the (constant) Newtonian viscosity and $v_r(r,z)$ is the radial fluid velocity. Combining the momentum balance with continuity,

$$\frac{1}{r}\frac{\partial (r v_r)}{\partial r} + \frac{\partial v_z}{\partial z} = 0, \tag{4}$$

results in the familiar parabolic flow profile and a net required force given by [22]

$$F_{\text{Newtonian}} = \frac{3}{2}\mu \frac{\dot{h}}{h}\pi R^2 \left(\frac{R}{h}\right)^2 \tag{5}$$

where the terms have been grouped to indicate that the adhesive force arises from a viscous stress ($\mu\dot{h}/h$) acting across the area πR^2, multiplied by the square of the aspect ratio $(R/h)^2$. A Newtonian fluid therefore acts as an adhesive but only in response to a dynamic situation with non-zero separation velocity $\dot{h}$.

A suitably non-Newtonian fluid such as a yield stress fluid [4, 5], can provide an adhesive force F even under *static* conditions [9]. Yield stress fluids (including magnetorheological fluids) are materials which approximately behave as a solid below a critical stress condition, flow as a liquid for larger stresses, and can repeatedly transition between these two states. Flow is typically assumed to occur when an invariant of the deviatoric stress tensor exceeds a critical value, $\frac{1}{2}\boldsymbol{\sigma'} : \boldsymbol{\sigma'} \geq \sigma_y^2$ [13, 25]. We are interested in surface separation with thin gaps ($h/R \ll 1$, see Fig. 2), in which the deformation is approximated as shear dominated. In this case the deviatoric stress for a viscoplastic fluid is also approximated as shear dominated with $\sigma_{zr} = \sigma_{rz}$ as the only non-zero components, and the yield criteria simplifies to $\sigma_{zr} \geq \sigma_y$. If the yield stress fluid is approximated as a perfectly plastic material with constant stress σ_y during flow (we will show rheological measurements to support this modeling approximation in Fig. 3) then the flow stress is independent of the shear-rate and therefore independent of the kinematics of deformation. For such a perfectly plastic yield stress material, fluid inertia is negligible compared to material stress if $\rho\dot{h}^2 R/\sigma_y h \ll 1$ (at most this ratio is $\sim 10^{-7}$ for our tests and we therefore neglect fluid inertia). The momentum balance in the r-direction is then determined from the free body diagram of Fig. 2b, and is given by

$$\frac{dp}{dr} = \frac{2\sigma_y(r)}{h}\text{sgn}(\dot{h}) \tag{6}$$

where h is the instantaneous height of the cylindrical fluid sample and $\text{sgn}(\dot{h})$ is used to achieve the appropriate sign for either squeeze flow ($\text{sgn}(\dot{h}) = -1$) or pull-off adhesion tests ($\text{sgn}(\dot{h}) = +1$). In the present study only "probe tack" adhesion tests are performed (tensile loading), for which $\text{sgn}(\dot{h}) = +1$. The yield stress may vary as a function of the radius, $\sigma_y(r)$, for example due to a nonhomogeneous magnetic field which activates the fluid (this is considered in the following section). For a passive perfectly plastic fluid, σ_y = constant throughout the entire fluid, and Eq. 6 can be integrated from the edge $r = R$ to arbitrary r, revealing a linear pressure profile. This pressure field is then integrated according to the vertical force balance (Eq. 2), giving the pull-off adhesion force for a perfect plastic fluid with constant yield stress,

$$F_{\text{YieldStress}} = \frac{2}{3}\sigma_y \pi R^2 \left(\frac{R}{h}\right) \tag{7}$$

where terms have been grouped to indicate a yield stress σ_y acting over the contact area πR^2 multiplied by the aspect ratio (R/h). This result assumes small gaps ($h/R \ll 1$), uniform fluid contact with the bounding surfaces, and a constant plastic yield stress σ_y which is independent of shear-rate. The material deformation is primarily shear and therefore adhesive performance relies on the magnitude of the shear yield stress.

We have considered various asymptotic limiting results for thin-gap fluid adhesion mechanisms (Eqs. 1, 5, 7) to give context to our results with a magnetorheological fluid (a viscoplastic fluid with a field-dependent yield stress). Note that each mechanism has a different sensitivity to the aspect ratio $(R/h)^k$, where $k = 0$ for capillary effects, $k = 1$ for yield stress fluids with constant flow stress, and $k = 2$ for viscous Newtonian fluids with constant viscosity. Furthermore, Newtonian fluid adhesion requires a finite separation velocity, whereas adhesive phenomena arising from capillarity or fluid yield stresses do not.

III. MODEL: MAGNETORHEOLOGICAL FLUID ADHESION WITH NONHOMOGENEOUS FIELDS

Here we extend the previous results of yield stress fluid adhesion discussed in Section II to include a radially dependent yield stress. We derive the resulting adhesive force for a field-dependent yield stress fluid subject to a nonhomogeneous magnetic field. The momentum balance in the z-direction (Eq. 2) and the r-direction (Eq. 6) presented above are still valid. Additionally, we must identify an appropriate constitutive equation relating shear yield stress to field strength and we must specify the configuration of the magnetic field.

The choice of constitutive equation is driven by experimental rheological measurements of the magnetorheological fluid (Fig. 3 and Fig. 4). For the fluid used here, a weak apparent shear yield stress, denoted σ_{y0}, exists in the ambient state even when no magnetic field is present. The shear yield stress increases in response to an external

magnetic field strength B (with field lines perpendicular to the shearing direction) according to a power law relationship. Up to moderate field strengths of $B \approx 0.2$ T, the constitutive equation relating shear yield stress to perpendicular external field strength can be written as

$$\sigma_y = \sigma_{y0} + \alpha B^2 \tag{8}$$

where $\sigma_{y0} \approx 6.24$ Pa and $\alpha = 137737$ Pa.T^{-2} are the measured values for the MR fluid used in our study (c.f. Fig. 3 and Fig. 4).

The final required input is the form of the magnetic field $B(r)$ which activates the MR fluid. Here we consider the case of a cylindrical permanent magnet (radius R_m, length L_m) which is offset from the fluid by a finite distance δ (Fig. 2). All other materials and structures in the setup are non-magnetic, and therefore have negligible influence on the magnetic field lines. The permanent magnet creates a nonhomogeneous magnetic field within the region of interest. For a given distance above the magnet, $\delta + h$, calculations indicate that the magnetic field strength is approximately constant for $r \leq R_m$, but decays as a power law $B \sim r^{-3}$ for $r > R_m$ (see Appendix D). Field lines are not strictly perpendicular to the shearing direction in this case, however, as a first order approximation we will neglect the field orientation and consider only spatial decay in the magnitude of the excitation field. The field magnitude can then be represented as

$$B(r) = \begin{cases} B_0 & r/R_m \leq 1 \\ B_0 \left(\frac{r}{R_m}\right)^{-3} & r/R_m \geq 1. \end{cases} \tag{9}$$

Equations 2, 6, 8, 9 can be combined to determine the adhesive force F resulting from the field-activated MR fluid setup. Two cases are distinguished. Case 1 will refer to the situation in which $R \leq R_m$, i.e. the fluid does not extend beyond the cross-sectional area of the magnet and is therefore activated by a constant magnetic field B_0. Case 2 will refer to $R \geq R_m$, in which the fluid at $r > R_m$ experiences a nonhomogeneous and decaying magnetic field strength.

For Case 1 ($R \leq R_m$) the shear yield stress is spatially homogeneous, $\sigma_y = \sigma_{y0} + \alpha B_0^2$ (Eq. 9). Integrating the momentum balance of Eq. 6 from R to r and using the boundary condition $p(R) = 0$ (neglecting surface tension effects) shows that the pressure field varies linearly in r,

$$p(r) = -\frac{2(\sigma_{y0} + \alpha B_0^2)}{h}(R - r), \tag{10}$$

and takes the maximum negative value at $r = 0$. This pressure field is then used in Eq. 2 to determine the force F acting on the top plate,

$$F = \frac{2}{3}(\sigma_{y0} + \alpha B_0^2)\pi R^2 \left(\frac{R}{h}\right). \tag{11}$$

which applies only for Case 1 with $R \leq R_m$ (note the similarity to Eq. 7 for a passive yield stress fluid with homogeneous yield stress).

For Case 2 ($R \geq R_m$) the same procedure is followed, but the nonhomogeneous magnetic field strength must be considered. For the region $0 \leq r \leq R_m$, the yield stress is constant, $\sigma_y = \sigma_{y0} + \alpha B_0^2$, and Eq. 6 is integrated from $r = R_m$ to arbitrary $r < R_m$ to find

$$p(r) = p(R_m) - \frac{2(\sigma_{y0} + \alpha B_0^2)}{h}(R_m - r), \quad \text{for } 0 \leq r \leq R_m \tag{12}$$

which is similar to Eq. 10 but includes the matching condition $p(R_m)$. The pressure field for $R_m \leq r \leq R$ is found by integrating Eq. 6 from $r = R$ to arbitrary $r > R_m$, using the boundary condition $p(R) = 0$. The momentum balance includes an inhomogeneous yield stress, and thus requires both the yield stress constitutive expression (Eq. 8) and the magnetic field condition (Eq. 9). Integration of Eq. 6 results in the following expression for the pressure field

$$p(r) = -\frac{2\sigma_{y0}}{h}(R - r) - \frac{2}{5}\alpha B_0^2 \frac{R_m}{h}\left[\left(\frac{r}{R_m}\right)^{-5} - \left(\frac{R}{R_m}\right)^{-5}\right], \quad \text{for } R_m \leq r \leq R. \tag{13}$$

The radial decay in the magnitude of the pressure for $r \geq R_m$ is very strong, since $dp/dr \sim \sigma_y \sim B^2 \sim (r/R_m)^{-6}$ in this region. The expressions for the pressure field (Eqs. 12 and 13) can then be used to determine the adhesive force F; first by using Eq. 13 to solve for the term $p(R_m)$, and then by substitution into and integration of Eq. 2. The expression for the resulting normal force F is

$$\frac{F}{F_m} = \begin{cases} \left(1 + \frac{\sigma_{y0}}{\alpha B_0^2}\right)\left(\frac{R}{R_m}\right)^3 & R/R_m < 1 \\ \left[2 - \left(\frac{R}{R_m}\right)^{-3} + \frac{\sigma_{y0}}{\alpha B_0^2}\left(\frac{R}{R_m}\right)^3\right] & R/R_m > 1 \end{cases} \tag{14}$$

where the characteristic force $F_m = \frac{2}{3}\alpha B_0^2 \pi R_m^2 (R_m/h_0)$ takes the form of an adhesive force for a yield stress fluid

(c.f. Eqs. 7 and 11). Note that the upper expression in Eq. 14, for $R/R_m < 1$, is equivalent to Eq. 11. This dimensionless form of Eq. 14 has been chosen as it is particularly convenient for considering both cases of $R/R_m < 1$ and $R/R_m > 1$.

For this yield stress fluid model, a finite force is required to initiate deformation. The peak force required to initiate deformation, F_{peak}, is a useful metric for the adhesive performance and is associated with the initial conditions $R = R_0$, $h = h_0$. The gain in adhesive performance associated with the MR response is determined by three dimensionless variables: R/R_m (the radial extent of the fluid sample compared to the size of the magnet), $\sigma_{y0}/\alpha B_0^2$ (the ratio of the ambient yield stress to the additional field-induced yield stress), and F/F_m (the dimensionless adhesive force).

For $R/R_m \leq 1$ the fluid experiences a homogeneous field strength B_0, and therefore exhibits a homogeneous yield stress. For this case the adhesive force is equivalent to the perfectly plastic yield stress fluid model (see Eq. 7), such that adhesive force increases as the cube of the fluid radius, $F \sim R^3$. For cases in which the fluid extends beyond the radius of the permanent magnet, $R_0/R_m > 1$, the activation field strength is nonhomogeneous, decreasing for $r > R_m$. Adding more fluid (increasing R_0/R_m) will increase the peak adhesive force but with weaker dependency on R_0/R_m.

Regarding the second dimensionless parameter, if $\sigma_{y0}/\alpha B_0^2 = 0$, the adhesive performance will asymptotically approach a constant value as $R_0/R_m \gg 1$, $F/F_m \to 2$. However, the MR fluid used in this study exhibits a finite apparent yield stress at zero field, $\sigma_{y0} \approx 6.24$ Pa. This off-state yield stress can dominate the response if $(\sigma_{y0}/\alpha B_0^2)(R/R_m)^3 \gg 2$, e.g. when the fluid extends far beyond the magnet.

IV. EXPERIMENTAL RESULTS

We have measured the material response in simple shearing deformation (shear rheometry) and normal force tensile adhesion (sometimes known as "probe tack" tests). Shear rheometry is used to measure the field-dependent shear yield stress, $\sigma_y(B)$, which is an input to the probe-tack adhesion models (Eqs. 7 and 14). Tensile adhesion experiments are performed on a separate linear force/displacement instrument with sensitive normal force resolution. Adhesive tensile tests are performed by separating the two disks at constant (apparent) speed $\dot{h}_A$, and the resulting force curves are measured. The apparent separation h_A is related to the true separation h via the instrument compliance [2], as outlined in Appendix A. The adhesive force predictions of Eqs. 7 and 14 are given for instantaneous values of fluid radius R and height h. In our experiments the fluid volume is constant, such that the instantaneous radius $R(t)$ is related to the instantaneous height $h(t)$,

$$R(t)^2 = \frac{R_0^2 h_0}{h(t)} \tag{15}$$

in which R_0 and h_0 are the initial values of fluid radius and height, respectively. Further details of the instrument setup and methods are given in Appendix A.

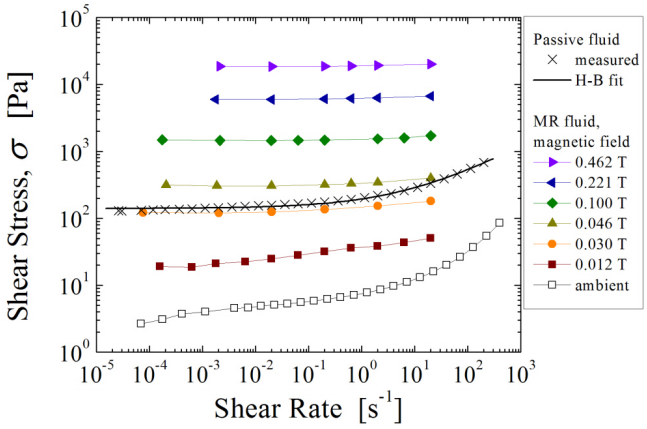

FIG. 3: Steady shear flow rheology of the experimental fluids. The passive yield stress fluid, aqueous Carbopol 2wt%, pH 7, is fit to the Herschel-Bulkley model (Eq. B1) with $\sigma_y = 140.0$ Pa, $K = 55.2$ Pa.s^n, and $n = 0.429$. The magnetorheological fluid approximately behaves as a perfectly plastic yield stress fluid with constant stress as a function of shear rate. Lines connect these MR fluid data points as a guide to the eye, and low rate yield stress values are extrapolated and shown in Fig. 4.

Two yield stress fluids are examined. We measured the steady shear flow rheology of each, as shown in Fig. 3. Each fluid exhibits a constant shear stress over a wide range of shear rates, and we interpret this stress plateau as the fluid yield stress σ_y. We first present adhesion measurements for a "passive" yield stress fluid which exhibits a significant yield stress without requiring a magnetic field ($\sigma_y \approx 140$ Pa). This serves as a starting point to show the signature of yield stress fluid adhesion and validate our experimental setup. The passive yield stress fluid is a water-based suspension of soft, water-swollen microgel particles (Carbopol 940, 2wt% in water), and has a consistency similar to a hair gel. Additional material information and rheometry details are given in Appendix B.

We then proceed to report our measurements of magnetorheological (MR) fluid adhesion and compare this to our model prediction (Eq. 14). A commercially available magnetorheological (MR) yield stress fluid is used, in which the ambient yield stress is small ($\sigma_{y0} \approx 6.24$ Pa) but can increase by several orders of magnitude in response to an external magnetic field. Fig. 3 gives the full steady shear rheology curves as a function of external magnetic field. The low-rate stress plateaus of Fig. 3 are interpreted as the static shear yield stress, and are

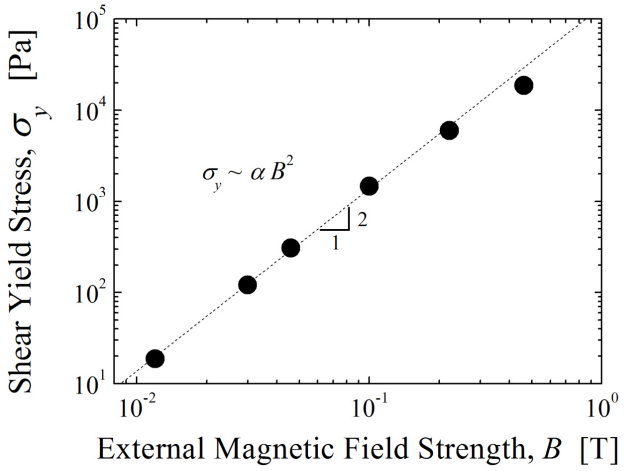

FIG. 4: Shear yield stress for the magnetorheological fluid as a function of the external magnetic field strength (field lines perpendicular to shearing direction). Yield stress values extracted from Fig. 3 (circles). The dashed line is a power law fit to the data (ignoring the data point at the largest field strength $B = 0.462$ T), resulting in $\alpha = 137737$ Pa.T^{-2}.

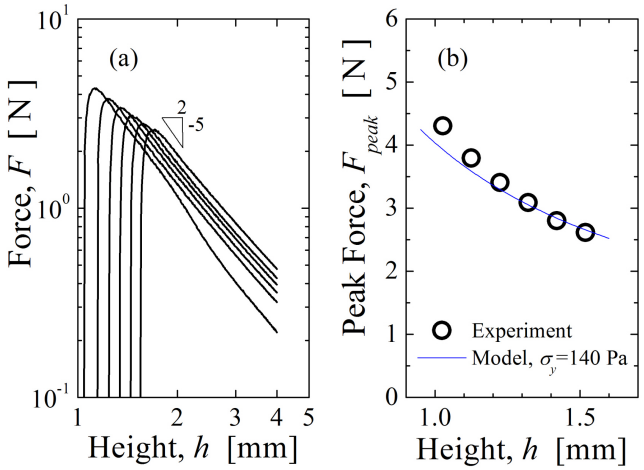

FIG. 5: Adhesive performance of the passive yield stress fluid, Carbopol 2wt%. The initial fluid thickness h_0 is varied for each test, whereas the initial fluid radius $R_0 = 24$ mm and plate speed $\dot{h}_A = 10$ μm/s are constant for all curves; (a) Force vs. displacement during pull-off, (b) Measured peak force compared to model prediction (Eq. 16).

plotted in Fig. 4 to show the measured shear yield stress dependence on external magnetic field. We observe a quadratic dependence $\sigma_y \sim B^2$ up to $B \approx 0.2$ T. Additional material details are given in Appendix B.

A. Passive yield stress fluid adhesion

Adhesive tensile tests for the passive yield stress fluid (Carbopol 940, 2wt%) are shown in Fig. 5, in which the gap height has been corrected for instrument compliance (the corrected height h is shown; see Appendix A for details of the compliance correction).

To prepare the adhesion experiment, the yield stress fluid is squeezed down to an initial height h_0 (see Appendix A for complete details). After squeezing we observe a residual negative force, due to compressing a fluid with a large yield stress. Once the pull-off test begins, the initial negative (compressive) force is released and the adhesive (tensile) force rapidly rises and reaches a maximum after a very small change in gap height. The rate of increase before the peak is likely due to elasticity in the material before yield, and the peak therefore represents the force required to yield and flow the material. After this maximum adhesive force the signal decays rapidly as the gap height increases. For this constant volume experiment the force can be written as a function of the initial geometry, R_0, h_0, and the instantaneous sample thickness h, by substituting the constant volume constraint of Eq. 15 into the force expression of Eq. 7, resulting in

$$F_{\text{YieldStress}} = \frac{2}{3}\sigma_y \pi R_0^2 \left(\frac{R_0}{h_0}\right)\left(\frac{h_0}{h}\right)^{5/2}. \qquad (16)$$

Notice here that the scaling relationship for constant volume deformation of a perfect plastic material is $F \sim h^{-5/2}$ (for a Newtonian fluid it would be $F \sim h^{-5}$, from Eqs. 5 and 15). The log-log plot of Fig. 5a shows that this scaling relationship holds for these tests, indicating perfectly plastic yield stress adhesion. The peak force is directly related to the adhesive performance. The experimentally measured peak force is compared to the model prediction (Eq. 16 evaluated at $h = h_0$) in Fig. 5b for various initial conditions. No fitting parameters are used here, since the geometry is known and the rheology was measured independently (Fig. 3). The model agrees well with experimental results. A small systematic deviation is apparent at the smallest initial gap heights h_0, which suggests a slight shear-rate dependence of the material stress since smaller initial gaps h_0 corresponds to higher characteristic shear rates, $\dot{\gamma} = \dot{R}/(h/2)$, i.e. higher initial characteristic shear rates $\dot{\gamma}_0 = \dot{h}R_0/h_0^2$. Such shear-rate dependence in the material stress is consistent with the rheological measurements of Fig. 3.

These results provide insight into yield stress fluid adhesion and serve as a starting point for understanding magnetorheological fluid adhesion. The correspondence between model and experiment for the passive yield stress fluid provides confidence that the experimental setup can be used to explore the unique situation of field-activated magnetorheological fluid adhesion against non-magnetic substrates.

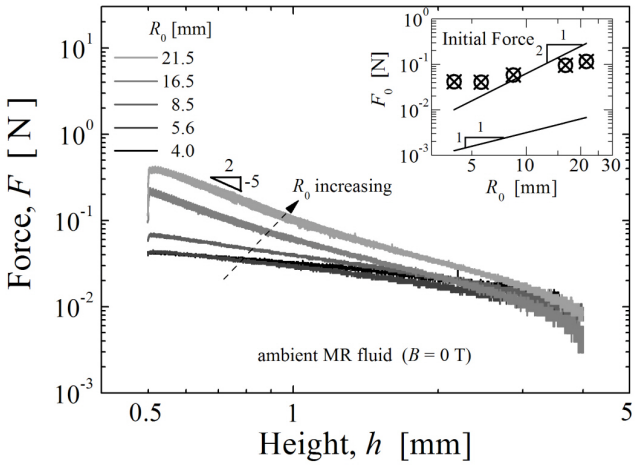

FIG. 6: Experimentally measured adhesive performance of the ambient MR fluid ($B_0 = 0$ T). Various initial fluid radii R_0 examined for the same separation speed $\dot{h}_A = 10\mu$m/s and initial height $h_0 = 0.5$ mm. The inset shows the measured initial static adhesive force F_0 which is attributed to capillary effects. Model lines show upper-bound estimates of Eq. 1 with $\gamma = 50$ mN/m for capillary adhesion originating from either a pressure jump at the interface (fully wetting, $\theta_E = 0°$, with log-log slope=2), or maximum line traction ($\theta_E = 90°$, with log-log slope=1).

B. Field-responsive magnetorheological fluid

Adhesive tensile tests for the MR fluid are performed in the same manner as described for the passive fluid. For field-activated adhesion tests, there is an additional step of introducing the permanent magnet after the fluid sample is squeezed to a thickness h_0.

Experimental results for the ambient MR fluid (no permanent magnet) are shown in Fig. 6, with tensile force F as a function of increasing gap height h. Here the initial fluid radius varies while all other test parameters are kept constant. The force approximately scales as $F \sim h^{-5/2}$ when the gap is sufficiently small ($h/R \ll 1$) which suggests yield stress fluid adhesion. This is consistent with the rheological observation that the MR fluid has a small apparent yield stress, even in the absence of an external magnetic field.

The initial force F_0 for these ambient tests is non-zero and positive, i.e. the fluid pulls downward on the upper plate (in contrast to the Carbopol tests in Fig. 5). We attribute this initial static adhesion to capillary effects, which become dominant over the material stresses as both yield stress σ_y and radius R decrease. The capillary force can be compared to the yield stress force by considering Eq. 1 and Eq. 7; taking the capillary pressure difference term of Eq. 1, the ratio is $F_{\text{Capillary}}/F_{\text{YieldStress}} = 3\gamma/\sigma_y R$. We can estimate this ratio with an upper bound estimate of surface tension $\gamma = 50$ mN/m for this oil-based fluid, $R = 21.5 - 4.0$ mm, and $\sigma_y = 6.24$ Pa for the ambient MR fluid. For the ambient tests of Fig. 6, the ratio $F_{\text{Capillary}}/F_{\text{YieldStress}} = 1.1 - 6$, indicating significant capillary effects.

A detailed account of capillary adhesion is beyond the scope of this work, and requires careful and precise experimental protocols to control details such as contact line pinning, interfacial curvature, and parallelism errors (we refer the reader to recent work such as [26]). These effects are negligible when the magnetic field is activated and the yield stress increases by several orders of magnitude; however, to illustrate that the deviations from our model predictions at small R_0 with the field off can be plausibly attributed to Capillary effects, we report the measured initial static force, shown as the inset of Fig. 6. The static force increases with fluid radius, and is compared to estimates of capillary force contributions using Eq. 1 with $\gamma = 50$ mN/m. The model lines consider separately the pressure differential and line traction contributions of Eq. 1, i.e. when contact angle $\theta_E = 0°$ and $\theta_E = 90°$, respectively. The contact angle at the edge of this viscous non-Newtonian fluid may vary due to pinning and we therefore consider these two extremes. The pressure drop effect is much larger than the maximum line traction for this geometry, and does a better job of estimating the order of magnitude of the initial static force F_0. However, the quantitative trend in the capillary-dominated regime does not precisely correspond with the simple theory of Eq. 1. We speculate that the lack of correspondence is due to uncontrolled contact line pinning, large initial gap, and possible parallelism errors. We will therefore subtract the initial static adhesive force to analyze the peak adhesive force, $F_{peak} - F_0$, in order to eliminate the static capillary force contribution and focus on the viscous contribution to adhesive performance. This correction is unnecessary for all other tests reported here, which have much larger yield stresses and therefore capillary forces are negligible, $F_{\text{Capillary}}/F_{\text{YieldStress}} \ll 1$. Indeed, an initial static adhesion was only observed for the ambient MR fluid with low yield stress.

Activating the MR fluid increases the adhesive force dramatically. Fig. 7 shows a representative set of force vs. displacement curves for the MR fluid activated by a moderate magnetic field $B_0 = 0.061$ T ($\sigma_y = 520$ Pa, $\sigma_{y0}/\alpha B_0^2 = 0.012$). Each curve corresponds to different values of R_0/R_m, with all other parameters held constant. A line representing $F \sim h^{-5/2}$ is shown for reference, which would be expected to apply for the cases with homogeneous shear yield stress ($R_0/R_m \leq 1$) and very small gaps $h/R \ll 1$. This is approximately the case as the plates begin to pull apart, indicating a fluid adhesive failure mechanism dominated by a yield stress. The maximum adhesive force occurs at the beginning of the pull-off test for each of these curves. Interestingly, for the curves with $R_0/R_m \geq 1$, the adhesive force peaks and is approximately constant over a range of h. This behavior is distinct from the passive yield stress fluid performance (Fig. 5), and may be related to the nonhomogeneous magnetic field condition, in which a reservoir

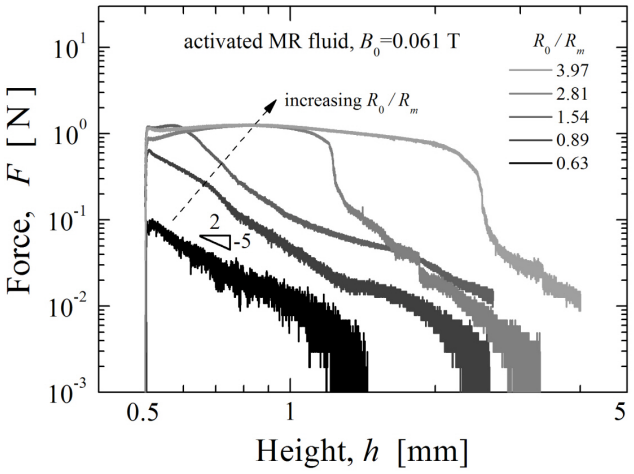

FIG. 7: Experimentally measured adhesive performance for a moderately activated MR fluid (Alnico 8 disc magnet, $B_0 = 0.061$ T). Various initial fluid radii, $4.0 \leq R_0 \leq 25.2$ mm, with magnet radius $R_m = 6.35$ mm. The separation speed $\dot{h}_A = 10\mu$m/s and initial height $h_0 = 0.5$ mm are the same for each curve.

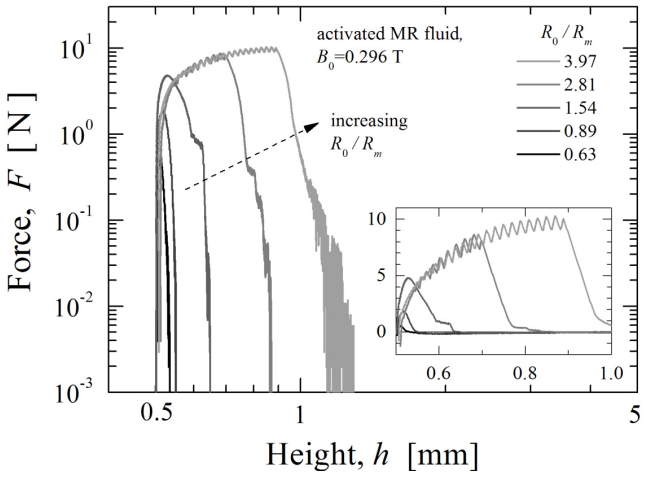

FIG. 8: Experimentally measured adhesive performance for a strongly activated MR fluid (Neodymium disc magnet, $B_0 = 0.296$ T). Various initial fluid radii, $R_0 = 4.0 - 25.2$ mm, with magnet radius $R_m = 6.35$ mm. The separation speed $\dot{h}_A = 10\mu$m/s and initial height $h_0 = 0.5$ mm are the same for each curve. The inset is a linear-linear plot of the same data, which highlights the iterative sawtooth failure leading up to the peak force (observed for $R_0/R_m = 2.81, 3.97$).

of "un-activated" fluid is available to be drawn into the region with approximately constant magnetic field B_0. The sustained magnitude of this tensile force makes the adhesive contact more robust. These results are representative of tests with moderate external magnetic fields, $B_0 < 0.1$ T.

An example of experimental measurements with a stronger magnetic field is shown in Fig. 8, in which $B_0 = 0.296$ T ($\sigma_{y0}/\alpha B_0^2 = 0.00052$). Just as in Fig. 7, the fluid radius R_0/R_m is varied while all other experimental parameters are held constant. The force vs. displacement curves for this case are quite different than those shown in Fig. 7. First, the peak adhesive force increases by a factor of 10 for comparable geometric parameters but stronger magnetic field. In Fig. 8 the peak stress does not occur near the initial gap height, rather the force grows to a maximum value at gap height $h^* > h_0$. Furthermore, a distinct sawtooth pattern can be seen in the curves for $R_0/R_m \geq 2.81$. The linear-linear plot in Fig. 8 (inset) highlights the sawtooth behavior. This sawtooth pattern is extremely repeatable, and performing successive tests on the same sample results in curves that are almost identical including even the phase of the sawtooth portion. We interpret this as a stick-slip phenomenon, for which a sufficient condition is a compliant drive component (our system stiffness $S = 124$ N/mm) and a static friction force that is higher than the kinetic friction force. For our case the slip seems to occur at the fluid/solid interface near the magnet – when viewed from below through the transparent bottom plate, the fluid radius R can be observed to "jump" at a frequency which corresponds with the sawtooth frequency. We observe that the force amplitude ΔF between peak and trough depends on the speed of separation, such that ΔF decreases as $\dot{h}$ increases, eventually leading to smooth force vs. displacement curves at a sufficiently large separation speed $\dot{h}$ (we observed smaller amplitude ΔF at $\dot{h} = 30\mu m/s$, but no stick-slip at $\dot{h} = 100\mu m/s$). This is consistent with the idea of a critical velocity to eliminate stick-slip behavior (e.g. see [27]). While sticking, the rise in force is related to the compliance of the instrument; the slope of this region is nearly linear and we observe $dF/dh_A \sim 70$ N/mm, which is slightly less than the instrument stiffness and indicates non-perfect sticking. We expect the drop in force during slip, ΔF, to occur over a timescale that depends on the system stiffness and the system inertia, $T = 2\pi/\omega$ with $\omega = \sqrt{S/M}$ (for underdamped slip [27]). For our system M is on the order of a few hundred grams, therefore the slip timescale is approximately $T \sim 0.01$ s which is lower than our measurement resolution $\Delta t = 0.15$ s. The stick-slip behavior should also depend on the surface roughness. Such detailed modeling is beyond the scope of this manuscript, however the sawtooth force curves can still be compared with other measurements and with the model proposed in Section III by considering the absolute maximum peak adhesive force for each curve.

In Figs. 9–10, the peak adhesive forces from multiple experimental measurements (beyond the representative force curves shown in Figs. 6–8) are compared with predictions of the model developed in Section III. The model (Eq. 14) is quantitatively predictive for the case of low to moderate field activation $B_0 < 0.1$ T with no fitting parameters (Fig. 9). In Fig. 9b it can be seen that the peak force increases as a function of the fluid radius, levels off

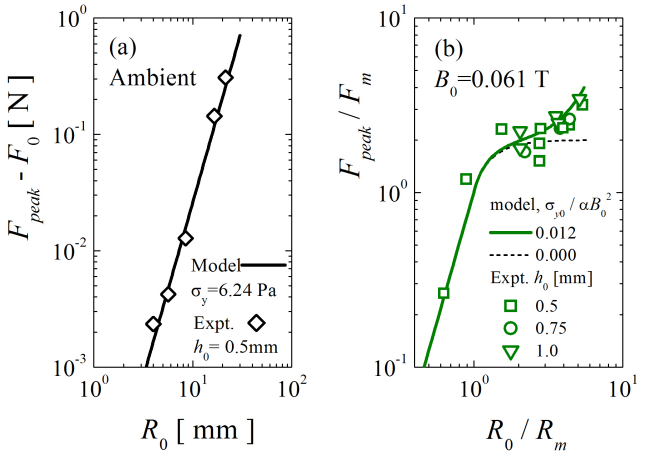

FIG. 9: Comparison between experimentally measured peak adhesive force with apparent speed $\dot{h}_A = 10$ μm/s (symbols) and model predictions (lines) at moderate magnetic field ($B_0 \leq 0.061$ T) with model parameters $\sigma_{y0} = 6.24$ Pa, $\alpha = 137737$ Pa.T^{-2}. (a) Ambient results (no magnet present) neglecting initial capillary force F_0, $B_0 = 0$ T from Fig. 6, compared to model prediction (Eq. 7). (b) Moderate magnetic field, $B_0 = 0.061$ T, for various initial geometries h_0 and (R_0/R_m) (see Fig. 7 for representative curves with $h_0 = 0.5$ mm). The theoretical predictions of the current model are given by the lines (Eq. 14). Model parameters are measured with independent tests, and therefore no adjustable parameters are used.

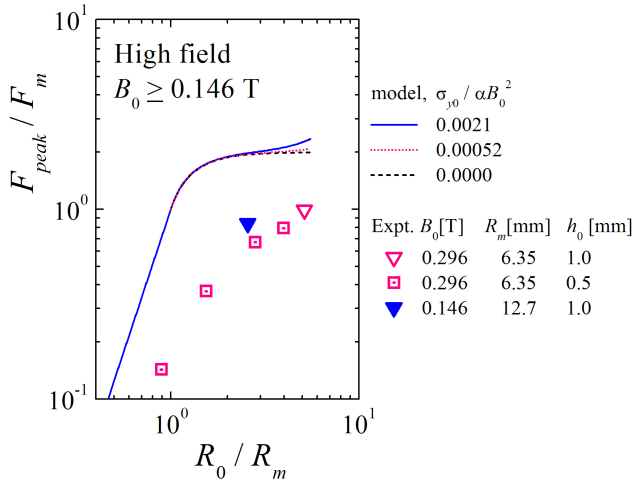

FIG. 10: High magnetic field ($B_0 \geq 0.146$ T) comparison between measured peak adhesive force (symbols) and model predictions ($\sigma_{y0} = 6.24$ Pa, $\alpha = 137737$ Pa.T^{-2}), for various initial geometries h_0 and (R_0/R_m). The theoretical predictions of the current model are given by the lines (Eq. 14). No fitting parameters are used. The experimentally measured adhesive strength is systematically lower than predicted by theory for these large field strengths.

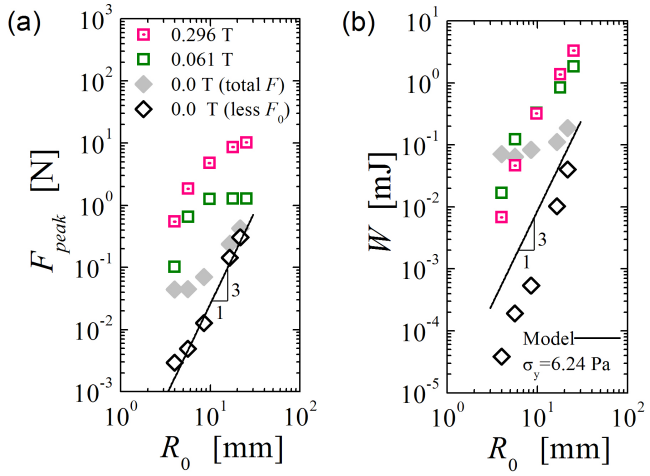

FIG. 11: Absolute measurement of adhesive performance in tension with a magnetorheological fluid, using data presented in Figs. 6–8. The model lines are for a homogeneous perfect plastic yield stress fluid with $\sigma_y = 6.24$ Pa, Eqs. 7 and 18. (a) Absolute measurement of peak tensile force F_{peak}, and (b) work of adhesion W for each experiment. The magnetic field is $B_0 = 0$ T (ambient), $B_0 = 0.061$ T, and $B_0 = 0.296$ T; each test uses initial fluid thickness $h_0 = 0.5$ mm. When present, the magnet radius is $R_m = 6.35$ mm.

as $R_0/R_m > 1$, and increases again at large R_0/R_m once the contribution from the static yield stress becomes significant.

For magnetic activation with higher fields ($B_0 > 0.146$ T), the model developed in Section III over-predicts the experimental measurements, as shown in Fig. 10. Some over-prediction would be expected for $B_0 > 0.2$ T due to the sub-quadratic scaling of the yield stress as the field is increased (Fig. 4), but this cannot completely account for the model discrepancy. Indeed, the experimental force vs. displacement curves presented in Fig. 8 show dramatically different behavior than those obtained at lower field activation. The failure mode under high field activation is characterized by the growth of adhesive force as the gap is increased, followed by the abrupt failure near the peak force. It is likely that interfacial failure (i.e. de-wetting or crack propagation at the fluid-surface interface) is occurring within these tests, which is not included in the current fluid flow model. It is common to use the terminology of "cohesive failure" (deformation and yielding within the bulk MR material) to contrast with "adhesive failure" (at the interface between the adhesive and the probe) [19]. The model here only considers cohesive failure, and any adhesive failure or detachment events would lower the total tensile force and reduce the performance predictions of the model.

Although the model over-predicts the peak adhesive force at the highest magnetic fields examined here (Fig. 10), we observe that the adhesive performance does continue to improve with increased magnetic field. Increasing the magnetic field strength increases the adhe-

sive force F_{peak} and also the measured work of adhesion

$$W = \int_{h_0}^{h_{\max}} F dh. \tag{17}$$

Fig. 11 summarizes the experimentally attainable tensile adhesion in terms of peak force F_{peak} and work of adhesion W. The data points in Fig. 11 are calculated for the representative experiments of Figs. 6–8, which used various magnetic field strength $B_0 = 0$ T, $B_0 = 0.061$ T, and $B_0 = 0.296$ T at constant initial fluid thickness $h_0 = 0.5$ mm. The work of adhesion is calculated using only the portion of the force curve with positive force $F(h) > 0$. For some magnetically activated cases we observed a negative initial force $F_0 < 0$ when the magnet was introduced. In our notation a negative force indicates fluid pushing the plates apart (Fig. 2), and our observation of an initial force pushing the plates apart is consistent with other experimental reports in the literature [28, 29]. We observe that the initial negative force quickly becomes positive as the plates are separated, i.e. becomes adhesive, resisting further separation in our notation. For the ambient experiments $B_0 = 0$ T, capillary forces contribute to an initial non-zero force adhesive force $F_0 > 0$ and analysis of peak force F_{peak} and work of adhesion W are performed on both the total force curves $F(h)$ (shown in Fig. 6) and also the shifted force curves calculated by subtracting the initial capillary force, $F(h) - F_0$, in order to focus on the viscous phenomenon ("less F_0" data in Fig. 11). The capillary effect is particularly apparent at smaller initial fluid radius R_0.

The absolute peak force F_{peak}, shown in Fig. 11a, climbs by about two orders of magnitude between the ambient state $B_0 = 0$ T and the maximum activated state $B_0 = 0.296$ T for a comparable area of contact. This increase in F_{peak} is monotonic for a given quantity of fluid, represented by initial fluid radius R_0. The work of adhesion W is shown in Fig. 11b, which is a measure of the total energy required to separate the two bounding surfaces. The work of adhesion W also climbs by about two orders of magnitude under strong magnetic activation.

The model line for work of adhesion $W_{\text{YieldStress}}$ in Fig. 11b is given for a perfect plastic yield stress fluid with homogeneous shear yield stress $\sigma_y = 6.24$ Pa (the ambient MR fluid with no magnet). The expression is given by

$$W_{\text{YieldStress}} = \frac{4}{9}\pi\sigma_y R_0^3 \tag{18}$$

which is found by substituting the expression for the tensile force exerted by a yield stress fluid, Eq. 16, into the work of adhesion definition, Eq. 17, and integrating from h_0 to ∞. For a yield stress fluid the work of adhesion is proportional to the cube of the contact radius, $W_{\text{YieldStress}} \sim R_0^3$, and the result for a Newtonian fluid is $W_{\text{Newtonian}} \sim R_0^4$ (this can be found from Eqs. 5 and 17). Some researchers may prefer to consider the work of adhesion per unit area, W/A with units mJ/mm^2. For example for disks of radius $R_0 = 20$ mm the work of adhesion (per unit area) for the MR fluid increases from $W/A = 1.3 \cdot 10^{-4}$ mJ/mm^2 with the field off (0.0 T with total force F) to a work of adhesion of $W/A = 1.5 \cdot 10^{-3}$ mJ/mm^2 with the field on ($B_0 = 0.296$ T). We also note that W/A is not constant for the viscous flow adhesion mechanisms discussed here, and that $W/A =$ constant would appear as a quadratic scaling $W \sim R_0^2$ in Fig. 11b.

It is noteworthy that capillary effects, via the initial static force F_0, seem to play an important role when looking at the work of adhesion W with small fluid radius R_0. At small radius R_0, the work of adhesion W calculated from the total force curves (filled symbols in Fig. 11b) can be larger for the ambient compared to the activated state. We attribute this larger work of adhesion to sustained fluid contact in the ambient case, which is shown in Fig. 6 by sustained force curves $F(h) > 0$ up to the maximum height tested, $h_{max} = 4$ mm. This is in contrast to the activated cases which exhibit a more pronounced adhesive failure and detachment of fluid, as observed in the force curves of Fig. 7 and Fig. 8, which can show an abrupt drop in force $F(h)$ at finite height $h < 4$ mm. For a sufficient quantity of fluid, $R_0 > 1$ mm, the initial static capillary force F_0 is less important, and the work of adhesion W monotonically increases as a function of magnetic field strength.

As the magnetic field strength is increased, fluid detachment limits the upper bound of adhesive performance with magnetorheological fluids – this seems to be why the model of Section III fails at high magnetic field. Despite that limitation, the presence of fluid detachment provides a unique advantage compared to other forms of fluid adhesion. Specifically, under certain circumstances, very little fluid is left on the substrate after pull-off. While the fluid is activated, the fluid is attracted to the magnetic field source. If forced detachment occurs, then the activated MR fluid can be pulled away and deadheres from the underlying substrate, sticking preferentially to the surface containing the magnetic field source. This is analogous to picking up iron filings with a permanent magnetic, but in this case one removes the bulk of a magnetic fluid adhesive. The remnant fluid adhering to the magnetic activation surface showed some remarkable regular patterns, including cusp-like "flower petals" in the fluid. See supplementary material at [URL will be inserted by AIP] for images of remnant fluid patterns.

V. CONCLUSIONS

We have experimentally demonstrated that field-activated magnetorheological (MR) fluids can be used for switchable normal force adhesion to non-magnetic substrates. The adhesion test apparatus allows one to vary and control the adhesive strength by varying the magnitude of the external magnetic field. A representative range of absolute adhesive performance is shown

in Fig. 11, demonstrating that MR fluid adhesive performance can be controlled over several orders of magnitude.

Our experimental data shows that MR fluid adhesive strength is determined by the yielding of the MR fluid flowing radially in a thin gap. To support this hypothesis we have developed a model of MR fluid adhesion under nonhomogeneous magnetic fields and compared this with experimental measurements. The comparison is satisfactory for moderate fields, in which we experimentally observe the force scaling ($F \sim h^{-5/2}$) predicted by the yield stress lubrication model. The model quantitatively describes the peak adhesive force for moderate magnetic field strengths $B < 0.1$ T with no free parameters. For stronger magnetic field $B_0 > 0.1$ T the adhesive force continues to increase with magnetic field strength, but additional modes of failure not captured in our simple model can occur. Consequently, the model over-predicts the adhesive performance for $B_0 > 0.1$ T. Guided by experimental observation we attribute this in part to wetting failure (i.e. debonding or crack propagation) at the bounding surface furthest from the magnet, which is influenced by the magnetic body force attracting the fluid toward the excitation magnet. Such attraction to the magnet is not detrimental, since in applications this may enable minimal residual material to be left behind after the adhesive contact is removed.

We anticipate that the topic of field-activated MR fluid adhesion will be a rich source of both scientific and engineering development in the future. Many unexplored parameters still exist for the problem of field-responsive magnetorheological fluid adhesion, such as substrate material, surface roughness, fluid thickness, magnetic field orientation, and other modes of adhesive failure such as peeling. Furthermore, a number of interesting phenomena can be explored in more detail in the future. This includes the stick/slip sawtooth waves observed in the force vs. displacement curves with strong magnetic fields (Fig. 8). This phenomenon can be examined by varying the instrument compliance, and is motivated by the possibility that the sawtooth wave may indicate the proximity to adhesive failure in a functional device. Additional phenomena include the over-prediction of peak forces for strong magnetic fields (Fig. 10) and the "flower" instability which is observed at moderate magnetic field strength [URL will be inserted by AIP].

Acknowledgments

We wish to acknowledge experimental assistance with MR fluid shear rheology from M. Ocalan. This material is based upon work supported in part by the U. S. Army Research Laboratory and the U. S. Army Research Office under contract/grant number W911NF-08-C-0055

APPENDIX A: INSTRUMENTATION

The shear rheology of the fluids is probed using the AR-G2 rotational rheometer (TA Instruments, New Castle, DE). The water-based passive yield stress fluid was tested with a plate-plate geometry (diameter $D = 40$ mm, gap $h = 1$ mm) using a solvent trap to mitigate evaporation. The magnetorheological fluid was also tested with a plate-plate geometry, with a gap of $h = 0.5$ mm. Ambient tests of the MR fluid used the standard rheometer setup and a top plate with $D = 40$ mm. To examine the magnetic field dependent rheology, a top plate with diameter $D = 20$ mm was used in concert with the MRF Rheometer Cell developed by Ocalan [30]. For both fluids, adhesive-backed waterproof sandpaper (600 grit McMaster Carr 47185A51) was attached to the top and bottom plates to help avoid slip at the bounding surfaces.

The parallel plate geometry imposes a nonhomogeneous strain field, with maximum strain at the edge of the plate ($r = R$). The material shear stress at the plate edge, σ_R, cannot be determined from a single torque measurement for a nonlinear material response. The true stress can be determined from $\sigma_R = \sigma_A \frac{1}{4}(3 + d\ln\sigma_A/d\ln\dot{\gamma}_R)$ (e.g. see Macosko [31]), where σ_R is the true stress at the edge of the disk and σ_A is the apparent stress determined by $\sigma_A = 2M/\pi R^3$ where M is the measured torque and R is the disk radius (the apparent stress calculation assumes a linear viscoelastic material response). Applying this correction requires derivatives of the apparent stress data. To calculate the required derivatives, we fit a fifth order polynomial function to the raw data of $\ln\sigma_A$ vs. $\ln\dot{\gamma}_R$, since this allows calculation of the derivative of a smooth analytical function rather than differentiating discrete raw data. This approach was applied to all rheological measurements.

The normal "pull off" adhesion was examined using a linear load/displacement instrument, the TA.XTplus Texture Analyzer (Stable Micro Systems, UK). The fluid is confined between two rigid surfaces. The top surface is an aluminum disk which can be displaced in the normal direction as shown in Fig. 2. This experiment is sometimes referred to as a "probe tack" test [19]. Adhesive-backed sandpaper (P2000 grit) was attached to the top plate unless noted otherwise. The fine grit gave reproducible results with minimum gap interference. The bottom plate is made of transparent plastic and can be accessed from below to introduce a permanent magnet. We have fabricated two bottom plate surfaces with different dimensions to allow for different size magnets and different magnet offset distances. One plate is solid polycarbonate of thickness 12.1 mm. The magnet is held to the bottom of the plate and separated from the fluid by a distance $\delta = 12.1$ mm. The plastic surface contacting the fluid is sandblasted to provide a finite roughness (r.m.s. roughness $R_q = 1.84\mu$m from 2D surface profilometry (Tencor P-11 Surface Profiler)). A second plate is made from transparent acrylic, thickness 8.3 mm, and

fabricated with a cylindrical hole in which a magnet can be placed $\delta = 1.0$ mm from the fluid (Fig. 2). For the MR fluid tests, the diameter of the top plate (typically $D = 48$ mm) is always bigger than the initial fluid diameter, which avoids the uncertainties associated with contact lines pinned to the edge of the plate. The MR fluid easily flows in the absence of a magnetic field, and an initial drop of known volume can be deposited with a pipette and subsequently squeezed into a disk shape. In contrast, the passive yield stress fluid does not flow easily. Consequently its volume is not easily allocated with a pipette and, furthermore, the "droplet" does not naturally take a disk shape when squeezed. To increase experimental precision in these tests, the fluid diameter and plate diameter are chosen to be the same, $D = 48$ mm, which ensures a proper initial condition of a disk shape with known radius. Here the passive yield stress fluid is deliberately overfilled so that excess material is squeezed out of all sides of the confinement space. Excess gel is then scraped away or "trimmed" using a blade so that the initial shape and the fluid radius can be precisely controlled.

The Texture Analyzer is known to exhibit finite compliance in the loading direction which can cause experimental artifacts under certain adhesive test conditions [2]. For our setup the system stiffness was measured to be $S = 0.124$ N/μm (Compliance $1/S = 8.08\mu$m/N). The stiffness was calibrated by placing the solid plates in contact and continuing to lower the drive motor (apparent height h_A). The stiffness is the magnitude of the slope dF/dh_A during plate contact, and was reasonably approximated as linear within our range of measurements. The system compliance is used to determine the true gap thickness, h, from the apparent gap thickness h_A according to $h = h_A - F/S$ where F is positive as defined in Fig. 2. Similarly for the true plate velocity, $\dot{h} = \dot{h}_A - \dot{F}/S$ where the over-dot represents a time derivative. For these tests the apparent gap h_A is the directly controlled parameter. All tests reported here were performed at constant apparent velocity $\dot{h}_A$.

The parallelism error of the bounding surfaces was also quantified. To measure the parallelism error, the top surfaces were bought into contact (gap $h = 0$) which occurs at a single contact point on the edge of the top plate. A gap will persist around the rest of the plate edge, and the maximum gap is measured by sliding gauge sheets of different thickness into the gap. Across the diameter of the $D = 48$ mm top plate, the maximum parallelism error is approximately $d \approx 127\mu$m, or an angle of $0.15°$. The minimum gap height used in these studies is $h = 400\mu$m, which represents the distance between the two nearest points on the bounding plates. All models in this work assume parallel surfaces; a detailed analysis of higher order effects due to non-parallel plates can be found, for example, in [32] for power-law fluids.

APPENDIX B: MATERIALS

The passive yield stress fluid is a water-based suspension of soft, water-swollen microgel particles, and has a consistency similar to a hair gel. The polymer microgel particles are available commercially under the name Carbopol 940, obtained from the Noveon corporation (Cleveland, OH). The Carbopol-based solution was prepared at a concentration of 2%(w/w), where w/w refers to weight of the additive with respect to the total weight of the mixture. The polymer was obtained as a white powder, and was added to deionized water being agitated with a magnetic stirrer. Samples were mixed for a minimum of 30 minutes. The Carbopol-water mixture initially has a pH near 3, and was neutralized with 4 M NaOH solution to achieve pH=7, producing a clear gel at the targeted concentration. The rheology of Carbopol mixtures depends on the pH, with maximum thickening occurring within a pH range of 6-7 [33].

Rheological measurements for the passive yield stress fluid (Carbopol) are presented in Fig. 3. These tests were performed by specifying the shear-rate (from high to low), in which case the instrument uses a control feedback loop to impose the appropriate torque. A rate-specified test was preferred here to correspond with the normal adhesion tests which also impose kinematic deformation conditions, i.e. displacement controlled tests. Furthermore, a rate-specified rheological test allows for the observation of a stress plateau across a broad range of shear-rates. Recent work has reported slow transients in shear flow of Carbopol (as long as 10^5 seconds) associated with shear-banding [34]. We also observed long transients and a lack of equilibrium, especially when the shear rate was ramped from low to high. Ramping shear rate down from high to low gave more reproducible results, but we note that slow transients could still be observed at the low shear rates when the "steady" shear stress was recorded, i.e. after waiting a maximum of 60 seconds at each data point.

The steady shear stress is shown as a function of shear-rate in Fig. 3. The Carbopol solution (X symbols) is not a perfectly plastic material. However, at low shear-rates the shear stress may be approximated as a plateau across several decades of shear-rate. The results across the entire range of shear-rates are fit to a Herschel-Bulkley model,

$$\sigma = \sigma_y + K\dot{\gamma}^n. \tag{B1}$$

resulting in $\sigma_y = 140.0$ Pa, $K = 55.2$ Pa.s^n, and $n = 0.429$ (shown in Fig. 3, solid line).

The field-active magnetorheological fluid was acquired from LORD Corp., (Cary, NC), available under the name MRF-132DG. The MR fluid is oil-based and contains carbonyl iron particles (1-20μm) at a volume fraction between 20%-40%, plus additives. The iron particles serve as magnetically-responsive constituents. An external magnetic field induces magnetic dipoles in the particles, causing them to form chains which dramatically

change the mechanical properties of the viscoplastic suspension.

The rheology of the MR fluid in steady shear flow (shear stress vs. shear rate) is shown in Fig. 3 for a range of magnetic field activation. The ambient state exhibits a broad stress plateau across several orders of magnitude in shear-rate, which serves as an apparent yield stress. Such a static yield stress is functionally useful for inhibiting the sedimentation of iron particles. For non-colloidal iron particles, the buoyant (or gravitational) force $(4/3)\pi a^3 \Delta\rho g$ must be smaller than the force available from the yield stress $\pi a^2 \sigma_y$, where $\Delta\rho$ is the density difference and a is the characteristic particle radius. We can estimate that a yield stress $\sigma_y \geq 1.8$ Pa is required for particles with $\Delta\rho = 6.87$ g/cm^3 and $a = 20\mu$m, and this criteria is satisfied by the MR fluid (Fig. 3). The MR fluid is not perfectly plastic, however, and the stress eventually increases as a function of shear-rate. As the magnitude of the magnetic field is increased, the yield stress increases and the MR fluid becomes more of a perfect plastic material, as evidenced by the flat stress profiles in Fig. 3.

The apparent yield stress is extracted from the corrected flow curves of Fig. 3. For the field-activated states, the yield stress is estimated from the average stress at the three lowest shear-rates. For the ambient response (open symbols), the effective yield stress may depend on the characteristic shear-rate. For instance, $\sigma_{y0} \approx 6.24$ Pa at a characteristic shear rate $\dot{\gamma} = \dot{h}R_0/h_0^2 = 0.254$ s^{-1}, which corresponds to the experimental parameters $h_0 = 0.5$ mm, $R_0 = 6.35$ mm, and $\dot{h} = 10\mu$m.s^{-1} used in Figs. 6–Fig. 8.

APPENDIX C: MR FLUID RATE DEPENDENT ADHESION

The influence of separation speed $\dot{h}_A$ is shown in Fig. 12. The force approximately scales as $F \sim h^{-5/2}$ when the gap is sufficiently small ($h/R \ll 1$) which suggests fluid adhesion dominated by yield stress. The weak rate dependence indicates that the off-state MR fluid is not a perfectly plastic material with constant flow stress, since the pull-off force slightly increases as a function of pull-off speed (this is consistent with rheological measurement shown in Fig. 3). Although the dependence is weak, the slowest pull-off speed available ($\dot{h}_A = 10\mu$m/s) is used in all subsequent tests to avoid artifacts related to speed. Fig. 12 includes a dashed line indicating the model prediction using a yield stress value $\sigma(\dot{\gamma} = 3.1\,\mathrm{s}^{-1}) = 7.99$ Pa. This stress (from linear interpolation of experimental data points in Fig. 3) corresponds to the characteristic shear-rate $\dot{\gamma} \approx \dot{h}R_0/h_0^2 = 1.5\,\mathrm{s}^{-1}$ for the conditions $\dot{h} = 10\mu$m/s, $R_0 = 24$ mm, $h_0 = 0.4$ mm.

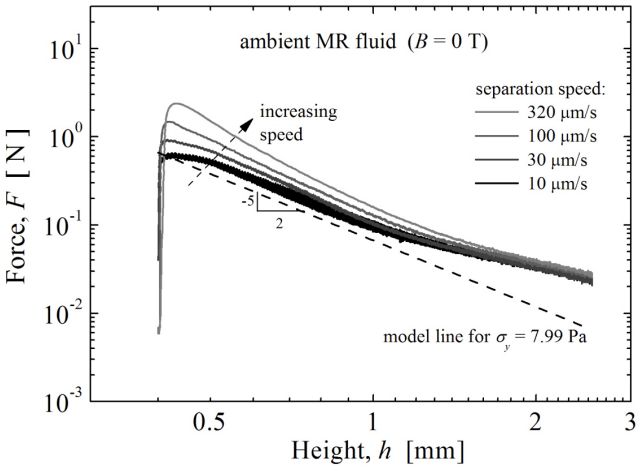

FIG. 12: Experimentally measured adhesive performance of the "off state" MR fluid. Various separation speeds are examined for the same initial radius $R_0 = 24$ mm and initial height $h_0 = 0.4$ mm. Here the dashed line is the prediction of the perfect plastic yield stress adhesion model with $\sigma_y = 7.99$ Pa, corresponding to the experimentally measured shear stress at the characteristic shear rate $\dot{\gamma} = \dot{h}R_0/h_0^2 = 1.5$ s^{-1}. The model line is shifted up to include the same initial force bias $F_0 = 0.083$ N as measured for the experiment at $\dot{h} = 10\mu$m/s. The top plate is the native aluminum surface.

APPENDIX D: MAGNETIC FIELD CONFIGURATION FOR PULL-OFF TESTS

Motivated by the utility of adhesion against an arbitrary substrate, we activate the fluid from only one side. Three different disc-shaped permanent magnets were used to activate the MR fluid. The weakest magnet is made from Alnico8, with radius $R_m = 6.35$ mm and length $L_m = 6.35$ mm. The magnetic strength was measured with a Hall effect probe (F.W. Bell, model #5180 Gauss/Tesla probe). Across the stand-off distance $\delta = 1.0$ mm, the measured field is $B = 0.059$ T at the center and $B = 0.061$ T on average near $R_m/2$ (four point average). For modeling and analysis, $B_0 = 0.061$ T is used to represent the field across the area of the magnet.

Neodymium magnets are used for the two strongest magnets. These are rare earth magnets comprised of neodymium, iron, and boron. The first of these has radius $R_m = 6.35$ mm and length $L_m = 9.5$ mm. Across the stand-off distance $\delta = 1.0$ mm, the field strength is measured to be $B = 0.319$ T at the center and $B = 0.296$ T on average near $R_m/2$. This final value is used to describe the field strength for adhesive tests, $B_0 = 0.296$ T. The final neodymium magnet is the largest, with radius $R_m = 12.7$ mm and length $L_m = 12.7$ mm. This magnet is used beneath the entire thickness of the bottom polycarbonate plate, with a stand-off distance $\delta = 12.1$ mm. At this distance the field measured at the center is $B = 0.163$ T, and the average

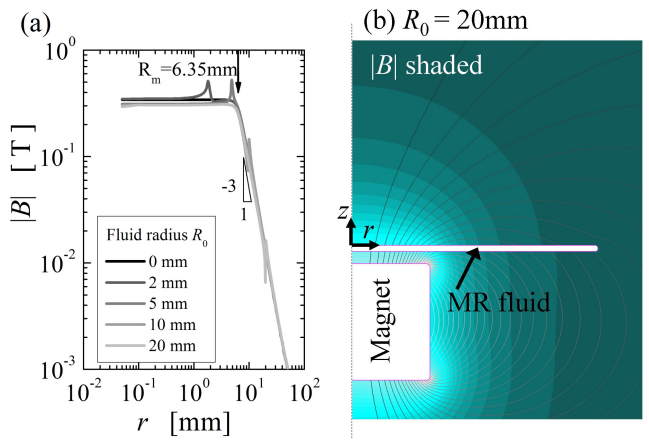

FIG. 13: Magnetic field profile for the Neodymium magnet, including the layer of magnetorheological fluid at various radii ($R_0 = 2, 5, 10, 20$ mm). The geometry is axisymmetric with a cylindrical polar coordinate system. (a) Magnitude of the external field on the top surface of the fluid, $|B|$ vs. r for z=constant. Localized spikes in the magnetic field occur near the edge of the fluid, but generally the profile is flat above the magnet ($r < R_m = 6.35$ mm) and decays as a cubic power law beyond the edge of the magnet ($r > R_m$). (b) Representative magnetic field in the r-z plane with fluid radius $R_0 = 20$ mm. Darker shading indicates lower external field $|B|$; flux lines are also shown.

field is $B = 0.146$ T. This final value is used as the field strength for MR fluid adhesive tests, $B_0 = 0.146$ T.

At sufficiently large distances ($r \gg R_m$) a cylindrical permanent magnet can be represented as a magnetic dipole. The magnetostatic problem for a magnetic dipole can be solved analytically only in the far field, in which case the magnetic field strength decays as $B \sim L^{-3}$, where L is the distance from the dipole (e.g. see [35]). The region of interest for our problem (Fig. 2) is close to the magnet and may be influenced by the presence of the MR fluid, and therefore the analytical solution does not strictly apply. The magnetic field was calculated using a finite element analysis (FEA) package, Maxwell SV (Ansoft, LLC, Pittsburgh, PA).

Results were obtained for the magnetostatic problem of a cylindrical permanent magnet with a thin, disk-shaped layer of MR fluid at a finite stand-off distance, δ, between the magnet and fluid (Fig. 13, c.f. Fig. 2). Representative results are presented in Fig. 13 for a Neodymium magnet with various quantities of MR fluid present. The radius of the cylindrical magnet is $R_m = 6.35$ mm, with length $L_m = 9.5$ mm. The geometry is axisymmetric with a cylindrical polar coordinate system. The magnet was modeled with a material selection option available in Maxwell SV (material 'NdFe30'). The presence of a magnetically permeable fluid will alter the magnetic field. FEA was used to examine this effect, using a fluid–magnet separation of $\delta = 1.0$ mm, a fluid thickness $h = 0.5$ mm, and various fluid radii ($R_0 = 2, 5, 10, 20$ mm). The fluid was modeled with a nonlinear B-H response curve as provided by the the fluid manufacturer. The plane of interest is the top surface of fluid, with $|B|$ shown in the vacuum outside of the fluid so that values may be compared with Hall probe measurements of the external field. The magnetic field at this location is of interest because it is furthest from the magnet and is likely to be the weakest link determining adhesion performance.

Fig. 13b shows a representative FEA calculation in the r-z plane, including both flux lines and the magnitude $|B|$ represented by shading. Fig. 13a gives $|B|$ vs. r for various cylindrical fluid volumes. In the presence of MR fluid, the magnetic field spikes near $r = R_0$ due to the curvature at the fluid boundary. In this case the fluid was modeled with rounded edges, with radius of curvature $h/2$. The most important feature of Fig. 13 is the observation that the magnitude of the field is approximately constant for $r \leq R_m$, but decays as a power law $B \sim r^{-3}$ for $r > R_m$. This decay coincides with the far field solution, and is confirmed by FEA calculations. These results were used in the model, Eq. 9.

[1] J. Stefan. Versuche ber die scheinbare adhsion. *Sitzungsberichte der Kaiserlichen Akademie der Wissenschaften, Mathematisch-Naturwissenschaftliche Classe*, 69:713–735, 1874.

[2] M. Tirumkudulu, W. B. Russel, and T. J. Huang. On the measurement of "tack" for adhesives. *Physics of Fluids*, 15(6):1588–1605, 2003.

[3] S. Poivet, F. Nallet, C. Gay, J. Teisseire, and P. Fabre. Force response of a viscous liquid in a probe-tack geometry: Fingering versus cavitation. *European Physical Journal E*, 15(2):97–116, 2004.

[4] H. A. Barnes. The yield stress - a review or 'pi alpha nu tau alpha rho epsilon iota' - everything flows? *Journal of Non-Newtonian Fluid Mechanics*, 81(1-2):133–178, 1999.

[5] D. Bonn and M. M. Denn. Yield stress fluids slowly yield to analysis. *Science*, 324(5933):1401–1402, 2009.

[6] M. W. Denny. The role of gastropod pedal mucus in locomotion. *Nature*, 285(5761):160–161, 1980.

[7] B. Chan, N. J. Balmforth, and A. E. Hosoi. Building a better snail: Lubrication and adhesive locomotion. *Physics of Fluids*, 17(11), 2005.

[8] R. H. Ewoldt, C. Clasen, A. E. Hosoi, and G. H. McKinley. Rheological fingerprinting of gastropod pedal mucus and synthetic complex fluids for biomimicking adhesive locomotion. *Soft Matter*, 3(5):634–643, 2007.

[9] D. Derks, A. Lindner, C. Creton, and D. Bonn. Cohesive failure of thin layers of soft model adhesives under tension. *Journal of Applied Physics*, 93(3):1557–1566, 2003.

[10] Q. Barral, G. Ovarlez, X. Chateau, J. Boujlel, B. Rabideau, and P. Coussot. Adhesion energy of soft-jammed systems. *Soft Matter*, 6:1343–1351, 2010.

[11] P. Coussot. Saffman-Taylor instability in yield-stress flu-

ids. *Journal of Fluid Mechanics*, 380:363–376, 1999.

[12] G. H. Meeten. Squeeze flow of soft solids between rough surfaces. *Rheologica Acta*, 43(1):6–16, 2004.

[13] J. Engmann, C. Servais, and A. S. Burbidge. Squeeze flow theory and applications to rheometry: A review. *Journal of Non-Newtonian Fluid Mechanics*, 132(1-3):1–27, 2005.

[14] B. Rabideau, C. Lanos, and P. Coussot. An investigation of squeeze flow as a viable technique for determining the yield stress. *Rheologica Acta*, 48(5):517–526, 2009.

[15] G. Ovarlez, Q. Barral, and P. Coussot. Three-dimensional jamming and flows of soft glassy materials. *Nature Materials*, 9:115–119, 2010.

[16] H. S. Tzou, H. J. Lee, and S. M. Arnold. Smart materials, precision sensors/actuators, smart structures, and structronic systems. *Mechanics of Advanced Materials and Structures*, 11(4-5):367–393, 2004.

[17] P. Kuzhir, M. T. Lopez-Lopez, G. Vertelov, C. Pradille, and G. Bossis. Shear and squeeze rheometry of suspensions of magnetic polymerized chains. *Rheologica Acta*, 47(2):179–187, 2008.

[18] S. A. Lira and J. A. Miranda. Field-controlled adhesion in confined magnetorheological fluids. *Physical Review E*, 80(4):046313, 2009.

[19] C. Gay and L. Leibler. On stickiness. *Physics Today*, 52(11):48–52, 1999.

[20] M. A. Fortes. Axisymmetric liquid bridges between parallel plates. *Journal of Colloid and Interface Science*, 88(2):338–352, 1982.

[21] M. J. Vogel and P. H. Steen. Capillarity-based switchable adhesion. *Proceedings of the National Academy of Sciences*, 107(8):3377–3381, 2010.

[22] L. D. Landau and E. M. Lifshitz. *Fluid mechanics*, volume 6 of *Course of theoretical physics*. Pergamon Press, New York, 2nd edition, 1987.

[23] B. A. Francis. *A study of fluid adhesion through application of a model tensile test*. PhD thesis, University of South Australia, 1999.

[24] B. A. Francis and R. G. Horn. Apparatus-specific analysis of fluid adhesion measurements. *Journal of Applied Physics*, 89(7):4167–4174, 2001.

[25] J. P. Singh and M. M. Denn. Interacting two-dimensional bubbles and droplets in a yield-stress fluid. *Physics of Fluids*, 20(4), 2008.

[26] Thomas Ward. Capillary-pressure driven adhesion of rigid-planar surfaces. *Journal of Colloid and Interface Science*, 354(2):816–824, 2011. 0021-9797 doi: DOI: 10.1016/j.jcis.2010.11.065.

[27] Alan D. Berman, William A. Ducker, and Jacob N. Israelachvili. Origin and characterization of different stick-slip friction mechanisms. *Langmuir*, 12(19):4559–4563, 1996. doi: 10.1021/la950896z 0743-7463 doi: 10.1021/la950896z.

[28] H. See and R. Tanner. Shear rate dependence of the normal force of a magnetorheological suspension. *Rheologica Acta*, 42(1-2):166–170, 2003.

[29] H. M. Laun, C. Gabriel, and G. Schmidt. Primary and secondary normal stress differences of a magnetorheological fluid (mrf) up to magnetic flux densities of 1 T. *Journal of Non-Newtonian Fluid Mechanics*, 148(1-3):47–56, 2008.

[30] M. Ocalan. Ph.D. thesis, Massachusetts Institute of Technology, in progress.

[31] C. W. Macosko. *Rheology: principles, measurements, and applications*. Advances in interfacial engineering series;. Wiley-VCH, New York, 1994.

[32] J. D. Sherwood. Squeeze flow of a power-law fluid between non-parallel plates. *Journal of Non-Newtonian Fluid Mechanics*, 166(5-6):289–296, 2011. 0377-0257 doi: DOI: 10.1016/j.jnnfm.2010.12.007.

[33] P. H. T. Uhlherr, J. Guo, C. Tiu, X. M. Zhang, J. Z. Q. Zhou, and T. N. Fang. The shear-induced solid-liquid transition in yield stress materials with chemically different structures. *Journal of Non-Newtonian Fluid Mechanics*, 125(2-3):101–119, 2005.

[34] T. Divoux, D. Tamarii, C. Barentin, and S. Manneville. Transient shear banding in a simple yield stress fluid. *Physical Review Letters*, 104(20):208301, 2010.

[35] R. P. Feynman, R. B. Leighton, and M. L. Sands. *The Feynman lectures on physics*, volume 2. Pearson/Addison-Wesley, San Francisco, definitive edition, 2006.